Interaction of two-dimensional atomic lattices with a single surface plasmon polariton

Rituraj [1], Meir Orenstein,[2] and Shanhui Fan[2,*]

[1]*Department of Electrical Engineering, Stanford University, Stanford, California 94305, USA*
[2]*Department of Electrical Engineering, Technion-Israel Institute of Technology, Haifa 32000, Israel*

We study the polaritonic bandstructure of a two-dimensional (2D) atomic lattice coupled to a surface plasmon polariton mode in the single excitation regime. We adopt a Dirichlet-to-Neumann map based computational technique which can accurately model non-Markovian dynamics as well as narrow-bandwidth features associated with any periodic atom-photon system in general. Using this technique, we design a 2D atomic lattice using only two-level atoms, which has an isolated flat polaritonic band where the magnitude of the group velocity for the modes in the band approach zero across the whole Brillouin zone. Such a system could be employed to slow, store, and manipulate single photons in a 2D geometry.

I. INTRODUCTION

The ability to manipulate atom-photon interactions has seen an unprecedented growth in recent decades enabling many technologies including but not limited to high precision metrology, quantum information processing and computing, and quantum memory. Starting from the initial demonstrations of using nanophotonic environment to control the radiative decay of an atom in the 1980s [1–3], we have come a long way and realized platforms allowing for design of new quantum selection rules for atomic transitions and even enabling conventionally forbidden multipolar and multiphoton processes [4–7]. Similar to the use of nanophotonic environment to control atomic states, atomic ensembles have also been employed to tailor light-matter interaction in processes such as photon blockade, sub- and super-radiance, nonlinear photon-photon interaction, photon bound states, electromagnetically induced transparency (EIT) etc. [8–17]. In recent years, ordered array of atoms interacting with few photons has garnered increasing attention and there have been several works showing effects arising from collective modes of atomic arrays. In particular, two-dimensional (2D) periodic arrays of atoms have been shown to exhibit subradiance [18–20], near perfect reflection of radiation [21,22], and long-lived topological excitations [23,24]. Experimentally, this could be realized on several platforms such as optical lattices formed by atoms, or artificial atoms (e.g., nitrogen-vacancy centers in diamond, superconducting qubits, or quantum dots) coupled with photonic structures [25–29].

However, the theoretical model associated with the periodic atomic lattice is typically obtained by tracing out the photon degrees of freedom in the Hamiltonian and applying the Markov approximation [19,30]. This approximation is not valid when the electromagnetic environment has narrow bandwidth features and is highly dispersive. The Markov approximation is also violated when the atom spacing becomes comparable to the wavelength of light in the structure, resulting in significant retardation effect due to photon propagation. Another almost universal assumption in these models is the electric dipole approximation for atomic transitions. In this work, we study the polaritonic band structure of 2D atomic lattice coupled to a surface plasmon polariton (SPP) mode [Fig. 1(a)] in the single excitation regime by applying a Dirichlet-to-Neumann (DtN) map based technique [31–33] (Here, we refer to both real atoms and atom-like objects as atoms.) The proposed framework is general and efficient for computing the properties of any 2D periodic system and does not suffer from the aforementioned approximations. We note that our treatment here is closely related to the treatment of an array of electromagnetic resonators interacting with an environment [34–36], where going beyond the Markov approximation is also important. This is particularly useful for studying resonant interaction with the SPP mode which is highly dispersive and has extremely small wavelengths near the surface plasmon frequency. Due to strong spatial confinement and large density of states near the surface plasmon frequency, the atom-SPP interaction strength is significantly enhanced which leads to a larger bandgap for the atomic lattice. We further exemplify the usefulness of this model by designing specific 2D atomic lattices with an isolated flat polaritonic band which can be possibly applied for slowing and storing single photons. This is achieved using arrays of two-level atoms and is different from the usual light slowing exhibited by EIT in an ensemble of three-level atoms [17,37–40]. The light-matter interaction which is already enhanced by the spatial confinement of the SPP modes is further substantially enhanced by the flat polaritonic band. This could provide an opportunity to tailor light-matter interactions such as allowing forbidden transitions, multiphoton processes and nonlinear optical effects. Similar photonic band structure may also be realized by employing arrays of optical resonators as illustrated by Yanik and Fan for a 1D system consisting of a

*shanhui@stanford.edu

waveguide side coupled to a periodic array of tunable optical resonators [41]. The atomic system however has several advantages as compared to the optical resonator system. Atoms outperform macroscopic optical resonators in terms of quality factor by several orders of magnitude, they are highly tunable, and are identical; a quality that is missing in fabricated optical resonators and severely impeding actual use of large resonator arrays. The intrinsic selection rules for atomic transitions can be further designed by employing artificial atoms (e.g., quantum dots) that provide an additional degree of freedom of control over light-matter interaction. Furthermore, the use of atomic arrays is a crucial step for quantum circuitry which engages between stationary (atoms) and flying qubits.

We note that throughout the paper we compute the properties of a single photon (or more precisely, a single plasmon-polariton) Fock state. As far as scattering properties are concerned, there are strong similarities between the scattering of a single photon against an atom, and a classical electromagnetic wave against a resonator, as can be deduced from many papers in waveguide quantum electrodynamics [42–45]. However, a single-photon Fock state is inherently a quantum object. Therefore, in the paper we use a full quantum treatment of photon-atom interaction to describe the properties of such a state.

The rest of the paper is organized as follows. In Sec. II, we describe the mathematical framework and derive an eigenvalue equation for bandstructure computation using the DtN technique. In Sec. III after a brief discussion of the band structure for a square lattice of atoms, we propose a periodic atomic structure with EIT-like unit cells [46], each containing two atoms, to get a gapped flat band. Subsequently, we design a unit cell structure exhibiting a Fano-like scattering spectrum that further substantially reduces the slope (group velocity) of the flat band. Finally, we illustrate a rich variety of phenomena resulting from a single SPP plane wave photon interacting with a finite lattice of Fano-like atomic unit cells at different frequencies. We conclude in Sec. IV.

II. MATHEMATICAL FORMULATION

Here, we develop the DtN map based formalism for computing the Bloch wave functions of a system composed of periodic lattice of identical two-level atom assembly coupled to a single photon in a 2D SPP mode. The DtN map is an operator which maps the field values at the unit cell boundary to its normal derivative [31–33]. A square lattice of atoms and its unit cell are shown schematically in Figs. 1(a) and 1(b), respectively. The infinite 2D surface that supports the SPP mode (shown in green) is taken to be the $z = 0$ plane and the atom (represented by a red cylinder) indexed by (u, v), is placed at the coordinates $(\mathbf{r}_{uv} \equiv (uD, vD), h)$, where D is the period of the square lattice and h is the atom-surface distance. We assume that the atoms are separated from the surface by vacuum, and the SPP mode is ideal without propagation losses. As we will see later in Sec. III C, a few lattice periods are enough to exhibit all the phenomena arising from the periodic structure and thus the lossless SPP model is a good approximation as long as the SPP propagation length is larger than few lattice periods. In the Coulomb gauge, the SPP vector potential operator $\mathbf{A}(\mathbf{r}, z)$ in the upper half space ($z > 0$) is
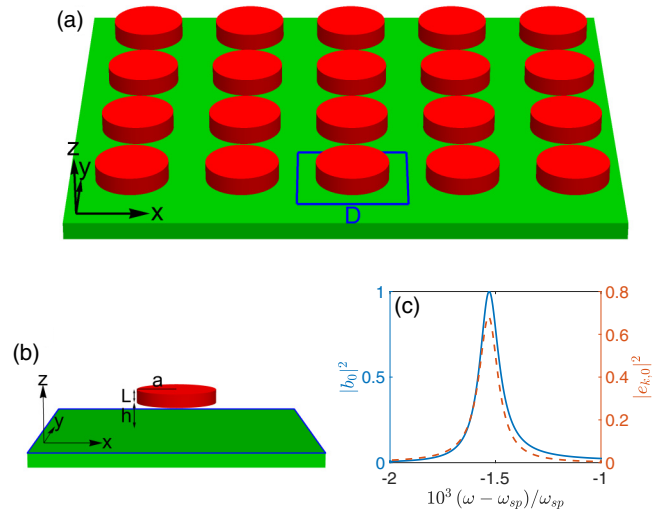

FIG. 1. (a) A square lattice of two-level atoms with period D, coupled to an SPP mode supported by the green surface, (b) Unit cell of the square lattice, (c) Scattering spectrum of an isolated atom. The solid blue and dashed red curves correspond to the scattered field amplitude squared $|b_0|^2$ and excited state population $|e_{k,0}|^2$, respectively.

given by [47–50]:

$$\mathbf{A}(\mathbf{r}, z) = \iint dk_x \, dk_y \, \underbrace{\frac{1}{2\pi} \sqrt{\frac{\hbar}{2L_\mathbf{k}\epsilon_0\omega_\mathbf{k}}} \left(i\hat{\mathbf{k}} - \frac{k}{\kappa}\hat{\mathbf{z}} \right) e^{-\kappa z} e^{i\mathbf{k}\cdot\mathbf{r}} a_\mathbf{k}}_{\mathbf{A}_\mathbf{k}(\mathbf{r}, z)}$$
$$+ \text{H.c.}, \tag{1}$$

where, $a_\mathbf{k}, a_\mathbf{k}^\dagger$ are the bosonic annihilation and creation operators for the SPP mode photon satisfying the commutation $[a_\mathbf{k}, a_{\mathbf{k}'}^\dagger] = \delta^2(\mathbf{k} - \mathbf{k}')$, $\hbar$ is the reduced Planck's constant, ϵ_0 is the vacuum permittivity, $\kappa = \sqrt{k^2 - \omega_\mathbf{k}^2/c^2}$ is the spatial decay rate of the mode along z, $L_\mathbf{k}$ is the characteristic modal dimension given by $L_\mathbf{k} = (\kappa^2 + k^2)/\kappa^3$ and is derived by normalization consideration, H.c stands for Hermitian conjugate. $\omega_\mathbf{k}$ is the SPP mode (angular) frequency for in-plane wave vector $\mathbf{k} \equiv (k_x, k_y)$, and could be well approximated for frequency close to the surface plasmon frequency ω_{sp} by

$$\omega_\mathbf{k} = \sqrt{\frac{1 + \epsilon_m}{\epsilon_m}} ck \approx \frac{\omega_p}{\sqrt{2}} \left(1 - \frac{k_p^2}{8k^2} \right) = \omega_{sp} - \frac{\beta}{k^2}, \tag{2}$$

where, ϵ_m is the real dielectric constant of the metal given by the Drude model, ω_p is its plasma frequency, k_p is the free space wave-vector magnitude at frequency $\omega_p(= ck_p)$, and c is the speed of light in vacuum [51–53].

A. System Hamiltonian model

We assume that the atoms couple only to the SPP mode and ignore coupling to the free-space electromagnetic modes as the near field coupling to the SPP modes is much stronger than coupling to the free-space modes. This assumption is further validated by the results presented later, where the linewidth associated with single SPP scattering by an atom is several

orders of magnitude larger than that for photon scattering in free space implying that the spontaneous emission into the SPP mode is much faster and probable. It is also assumed that the atoms do not directly (electronically) interact with each other. Starting with the standard minimal coupling Hamiltonian, for resonant coupling near the surface plasmon frequency, we can show that the light-matter interaction in the atom-SPP system can be described by the following spatial domain Hamiltonian [46,54]:

$$
\begin{aligned}
H = {} & \hbar\omega_{sp} \iint dx\,dy\, c^\dagger(\mathbf{r})c(\mathbf{r}) + \hbar\beta \iint dx\,dy \\
& \times \iint dx'\,dy' \frac{\ln|\mathbf{r}-\mathbf{r}'|}{2\pi} c^\dagger(\mathbf{r})c(\mathbf{r}') \\
& + \sum_u \sum_v \bigg(E_g f_{guv}^\dagger f_{guv} + E_e f_{euv}^\dagger f_{euv} \\
& + \iint dx\,dy (V_{uv}(\mathbf{r})c^\dagger(\mathbf{r})f_{guv}^\dagger f_{euv} + \text{H.c}) \bigg),
\end{aligned}
\tag{3}
$$

where, E_g and E_e are the atomic ground and excited state energies, and f_{guv}, $f_{guv}^\dagger$, f_{euv}, $f_{euv}^\dagger$ are the respective fermionic annihilation and creation operators for the electron in the atom (u, v). $c(\mathbf{r})$, $c^\dagger(\mathbf{r})$ are the spatial bosonic annihilation and creation operators, respectively, as defined by Eq. (4) and satisfy the commutation $[c(\mathbf{r}),\ c^\dagger(\mathbf{r}')] = \delta^2(\mathbf{r}-\mathbf{r}')$. $V_{uv}(\mathbf{r})$ is the Fourier transform of the atom-field coupling strength $V_{\mathbf{k}}^{uv}$ given by Eq. (5):

$$
c(\mathbf{r}) = \frac{1}{2\pi} \iint dk_x\,dk_y\, e^{i\mathbf{k}\cdot\mathbf{r}} a_{\mathbf{k}};
$$

$$
c^\dagger(\mathbf{r}) = \frac{1}{2\pi} \iint dk_x\,dk_y\, e^{-i\mathbf{k}\cdot\mathbf{r}} a_{\mathbf{k}}^\dagger,
\tag{4}
$$

$$
V_{\mathbf{k}}^{uv*} = -\frac{e}{m} \langle e_{uv}|\mathbf{A}_{\mathbf{k}}\cdot\mathbf{p}_{uv}|g_{uv}\rangle;
$$

$$
V_{uv}(\mathbf{r}) = \frac{1}{2\pi} \iint dk_x\,dk_y\, e^{i\mathbf{k}\cdot\mathbf{r}} V_{\mathbf{k}}^{uv},
\tag{5}
$$

where, e and m are, respectively, the charge and the rest mass of the electron, $\mathbf{p}_{uv} = -i\hbar\vec{\nabla}_{uv}$ is the canonical momentum operator for the electron in the atom (u, v). In the Hamiltonian of Eq. (3), we have ignored the terms related to intrinsic spin angular momentum and the $\mathbf{A}^2$ term. We have also made the usual rotating wave approximation in the interaction Hamiltonian [55–57]. These approximations are justified in the weak coupling regime (small $V_{\mathbf{k}}$) [54], which is the case here as we have a single photon interacting with a low density atomic lattice such that the period is significantly larger than the size of the atoms. The logarithmic form in the second term of the Hamiltonian of Eq. (3) arises from the SPP dispersion relation in the short wavelength limit [Eq. (2)]. Since all the atoms are identical, from Eq. (5), $V_{\mathbf{k}}^{uv} = e^{-i\mathbf{k}\cdot\mathbf{r}_{uv}} V_{\mathbf{k}}^{00}$ which arises from the periodicity condition $V_{uv}(\mathbf{r}) = V_{00}(\mathbf{r} - \mathbf{r}_{uv})$. To compute the band structure, we look for Bloch eigenstates of the form:

$$
\begin{aligned}
|\psi_{\mathbf{q}}\rangle = {} & \iint dx\,dy\, \phi_{\mathbf{q}}(\mathbf{r})c^\dagger(\mathbf{r}) |g, g, \ldots, 0\rangle \\
& + \sum_u \sum_v e_{\mathbf{q}}^{uv} f_{euv}^\dagger f_{guv} |g, g, \ldots, 0\rangle,
\end{aligned}
\tag{6}
$$

where, $|g, g, \ldots, 0\rangle$ is the state with all atoms in the ground state and zero photons in the SPP mode, $\mathbf{q}$ is the Bloch wave vector, $\phi_{\mathbf{q}}(\mathbf{r})$ is the photon field amplitude, and $e_{\mathbf{q}}^{uv}$ is the excited state amplitude for the atom (u, v). Equation (6) represents a complete basis for the system [42,58]. Following from the Bloch condition:

$$
\phi_{\mathbf{q}}(\mathbf{r} + \mathbf{r}_{uv}) = e^{i\mathbf{q}\cdot\mathbf{r}_{uv}} \phi_{\mathbf{q}}(\mathbf{r}),
\tag{7a}
$$

and

$$
e_{\mathbf{q}}^{uv} = e^{i\mathbf{q}\cdot\mathbf{r}_{uv}} e_{\mathbf{q}}^{00}.
\tag{7b}
$$

We assume that the atom-field interaction is local, i.e., $V_{uv}(\mathbf{r}) = 0$ for $|\mathbf{r} - \mathbf{r}_{uv}| > D/2$. Thus, it is possible to compute the Bloch state and the band structure from the knowledge of scattering properties of an isolated unit cell coupled to a SPP mode of an infinite 2D surface.

The isolated atom scattering is computed by the procedure outlined in a previous work [54] and is shortly described here. We model the two-level atom as an infinite potential well confining the electron in a cylinder of radius a and height L as shown in Fig. 1(b) with the following wave functions for the ground ($l_g = 1$) and excited ($l_e = 2$) states of atom $(0, 0)$:

$$
\begin{aligned}
\psi_{g,e}(\mathbf{r}, z) = {} & \sqrt{\frac{2}{L}} \sin\frac{l_{g,e}\pi(z-h)}{L} \\
& \times \frac{1}{\sqrt{\pi}aJ_1(j_0)} J_0(j_0 r/a)\Theta(r, z),
\end{aligned}
\tag{8}
$$

where, J_n is the nth order Bessel function, j_n is the nth zero of the 0th order Bessel function, $\Theta(r, z)$ is a scalar function which is unity inside the cylinder ($r < a$, $h < z < h + L$) and zero outside [59]. In this case, $V_{00}(\mathbf{r})$ has azimuthal symmetry [Eq. (5)], making it convenient to work using cylindrical coordinates (r, θ, z). Now, the scattering eigenstates of an isolated atom at SPP wave-vector magnitude k (frequency ω_k) and angular momentum $m\hbar$ is given by

$$
|\psi_{k,m}\rangle = \iint dx\,dy\, \phi_{k,m}(\mathbf{r})c^\dagger(\mathbf{r}) |g, 0\rangle + e_{k,m}^{00} f_{e00}^\dagger f_{g00} |g, 0\rangle.
\tag{9}
$$

Away from the atom, in the far field the photon field $\phi_{k,m}(\mathbf{r})$ could be represented as a sum of incident and scattered waves as given by Eq. (10a), where $H_m^{(1)}$ is the Hankel function of the first kind of order m and b_m is the corresponding scattering coefficient. The excited state amplitude $e_{k,m}$ is given by Eq. (10b). Following from the azimuthal symmetry of $V_{00}(\mathbf{r})$, $e_{k,m} = 0$ for $m \neq 0$. Thus, the atom only scatters the $m = 0$ angular momentum mode, i.e., $b_m = 0$ for $m \neq 0$, which is also expected from the conservation of angular momentum. The only nonzero scattering coefficient b_0 is computed using appropriate boundary conditions as done in the previous work [54]:

$$
\phi_{k,m}(\mathbf{r}) = J_m(kr)e^{im\theta} + b_m H_m^{(1)}(kr)e^{im\theta},
$$
$$
-\infty \leqslant m \leqslant \infty,
\tag{10a}
$$

$$
(\hbar\omega_k + E_g - E_e)e_{k,m} = \iint dx\,dy\, V_{00}^*(\mathbf{r})\phi_{k,m}(\mathbf{r}).
\tag{10b}
$$

Having computed the scattering eigenstates of an isolated unit cell, we use the DtN map based technique to compute the band structure of the infinite periodic lattice. The procedure is general and applicable for other types of 2D lattices as well as more complicated unit cells containing more than one atom. Here we assume a simplified model for the atomic potential in order to obtain an easy-to-use analytic expression for the electronic wave functions. In general, the formalism can be used to treat more realistic atomic models by incorporating the actual electronic wave functions of the atoms.

In the following, we first illustrate in Sec. II B an efficient way to compute the DtN map by expanding the field in terms of the cylindrical waves. Then using the computed DtN map, in Sec. II C we formulate an eigenvalue equation in terms of Bloch wave vector to compute the band structure.

B. Computing DtN map

Since, the atoms do not interact directly with each other, the photon field $\phi_\mathbf{q}(\mathbf{r})$ [Eq. (6)] inside each unit cell can be expressed in terms of the local cylindrical wave solutions $\phi_{k,m}(\mathbf{r})$, obtained for an isolated atom [Eq. (10)]. Note that, the Bloch wave vector magnitude q is in general different from the SPP wave vector magnitude k.

$$\phi_\mathbf{q}(x, y) = \sum_{m=-\infty}^{\infty} c_m \phi_{k,m}(r, \theta), \quad -D/2 \leqslant x, y \leqslant D/2 \tag{11}$$

The DtN map, Λ, of the unit cell is defined through:

$$\Lambda(u_0, v_0, u_1, v_1)^T = (\partial_y u_0, \partial_x v_0, \partial_y u_1, \partial_x v_1)^T, \tag{12}$$

where, u_0, v_0, u_1, and v_1 are the values of the photon field $\phi_\mathbf{q}(x, y)$ on the four edges of the square unit cell:

$$u_0 = \phi_\mathbf{q}(x, -D/2), \quad v_0 = \phi_\mathbf{q}(-D/2, y),$$
$$u_1 = \phi_\mathbf{q}(x, D/2), \quad v_1 = \phi_\mathbf{q}(D/2, y),$$
$$\partial_y u_0 = \partial_y \phi_\mathbf{q}|_{y=-D/2}, \quad \partial_x v_0 = \partial_x \phi_\mathbf{q}|_{x=-D/2},$$
$$\partial_y u_1 = \partial_y \phi_\mathbf{q}|_{y=D/2}, \quad \partial_x v_1 = \partial_x \phi_\mathbf{q}|_{x=D/2}.$$

As a discrete approximation, we select N points on each edge of the unit cell:

$$x_j = y_j = (j - N/2 + 0.5) \times L/N, \quad j = 0, 1, \ldots, N-1,$$

and replace u_0, v_0, u_1, v_1 by column vectors of length N. The DtN map Λ can now be represented by a $4N \times 4N$ matrix obtained by truncating the infinite cylindrical wave basis to a finite set of size $4N$ and approximating Eq. (11) as

$$\phi_\mathbf{q}(x, y) \approx \sum_{m=-2N}^{2N-1} c_m \phi_{k,m}(r, \theta). \tag{13}$$

We follow a two step strategy to compute the approximate matrix operator corresponding to the DtN map Λ. First, we compute a $4N \times 4N$ matrix Λ_1 which maps the $4N$ cylindrical wave coefficients to the field values at the $4N$ points on the unit cell boundary. This can be easily done by evaluating the known cylindrical waves $\phi_{k,m}(r, \theta)$, $-2N \leqslant m \leqslant 2N-1$ at the points on the unit cell boundary $\{(x_j, \pm D/2), (\pm D/2, y_j)\}$, $j = 0, 1, \ldots, N-1$. In the next step, we similarly compute another operator Λ_2 to map the cylindrical wave coefficients to the normal derivative of the field at the points on the unit cell boundary. The DtN map Λ can then be expressed as

$$\Lambda = \Lambda_2 \Lambda_1^{-1}. \tag{14}$$

C. Eigenvalue problem

Having computed the DtN map Λ at a given SPP wave-vector magnitude k (or, frequency ω_k), we need to compute the unknown Bloch wave vector $\mathbf{q} \equiv (q_x, q_y)$ satisfying the Bloch conditions given by Eqs. (7a) and (7b). Equation (7b) follows from Eq. (7a) as evident from Eq. (10b) and thus we only need to enforce the Bloch criterion for the photon field. Expressing the Bloch condition in Eq. (7a) in terms of the field values at the unit cell boundary:

$$\phi_\mathbf{q}(x, D/2) = \rho_y \phi_\mathbf{q}(x, -D/2),$$
$$\partial_y \phi_\mathbf{q}|_{y=D/2} = \rho_y \partial_y \phi_\mathbf{q}|_{y=-D/2}, \tag{15a}$$
$$\phi_\mathbf{q}(D/2, y) = \rho_x \phi_\mathbf{q}(-D/2, y),$$
$$\partial_x \phi_\mathbf{q}|_{x=D/2} = \rho_x \partial_x \phi_\mathbf{q}|_{x=-D/2}, \tag{15b}$$

where, $\rho_x = e^{iq_x D}$ and $\rho_y = e^{iq_y D}$. Rewriting Eq. (12) by partitioning the DtN matrix Λ in 4×4 blocks, we get

$$\begin{bmatrix} \Lambda_{11} & \Lambda_{12} & \Lambda_{13} & \Lambda_{14} \\ \Lambda_{21} & \Lambda_{22} & \Lambda_{23} & \Lambda_{24} \\ \Lambda_{31} & \Lambda_{32} & \Lambda_{33} & \Lambda_{34} \\ \Lambda_{41} & \Lambda_{42} & \Lambda_{43} & \Lambda_{44} \end{bmatrix} \begin{bmatrix} u_0 \\ v_0 \\ u_1 \\ v_1 \end{bmatrix} = \begin{bmatrix} \partial_y u_0 \\ \partial_x v_0 \\ \partial_y u_1 \\ \partial_x v_1 \end{bmatrix}. \tag{16}$$

Now, from Eqs. (15) and (16), we obtain

$$\begin{bmatrix} \Lambda_{31} & \Lambda_{32} \\ \Lambda_{41} & \Lambda_{42} \end{bmatrix} \begin{bmatrix} u_0 \\ v_0 \end{bmatrix} = \begin{bmatrix} \rho_y^2 \Lambda_{13} + \rho_y(\Lambda_{11} - \Lambda_{33}) & \rho_y \rho_x \Lambda_{14} - \rho_x \Lambda_{34} + \rho_y \Lambda_{12} \\ \rho_y \rho_x \Lambda_{23} + \rho_x \Lambda_{21} - \rho_y \Lambda_{43} & \rho_x^2 \Lambda_{24} + \rho_x(\Lambda_{22} - \Lambda_{44}) \end{bmatrix} \begin{bmatrix} u_0 \\ v_0 \end{bmatrix}. \tag{17}$$

Eq. (17) could be cast as an eigenvalue problem with eigenvalue λ. We illustrate this for Bloch wave vector lying along the ΓM direction ($q_x = q_y$) in the irreducible Brillouin zone with corners at $\Gamma(q_x = q_y = 0)$, $X(q_x = \pi/D, q_y = 0)$, and $M(q_x = q_y = \pi/D)$. Substituting $\rho_x = \rho_y = \lambda$, and $(u_0, v_0)^T = \mathbf{U}$ in Eq. (17), we get the following eigenvalue equation:

$$(\lambda^2 A + \lambda B + C)\mathbf{U} = 0, \tag{18}$$

where, $A = -\begin{bmatrix} \Lambda_{13} & \Lambda_{14} \\ \Lambda_{23} & \Lambda_{24} \end{bmatrix}$, $B = \begin{bmatrix} \Lambda_{33} - \Lambda_{11} & \Lambda_{34} - \Lambda_{12} \\ \Lambda_{43} - \Lambda_{21} & \Lambda_{44} - \Lambda_{22} \end{bmatrix}$, and $C = \begin{bmatrix} \Lambda_{31} & \Lambda_{32} \\ \Lambda_{41} & \Lambda_{42} \end{bmatrix}$.

For any direction in the Brillouin zone, we always get an eigenvalue equation of the form given in Eq. (18) but with different expressions for A, B, C, and λ. The eigenvalue equation is quadratic in λ and can be linearized by introducing an auxiliary

vector $\mathbf{V} = \lambda\mathbf{U}$:

$$\lambda\begin{bmatrix} A & 0 \\ 0 & I \end{bmatrix}\begin{bmatrix} \mathbf{V} \\ \mathbf{U} \end{bmatrix} + \begin{bmatrix} B & C \\ -I & 0 \end{bmatrix}\begin{bmatrix} \mathbf{V} \\ \mathbf{U} \end{bmatrix} = 0. \qquad (19)$$

Since propagating Bloch waves have real $\mathbf{q}$, the eigenvalue $\lambda = e^{iq_x D}$ has unit amplitude inside a band and is different from unity in a band gap.

The procedure outlined above is different from the usual band-structure computation where the eigenvalue problem is formulated for a given Bloch vector and yields ω^2 (ω is the frequency) as the eigenvalue. Here, the DtN map is computed for a given SPP frequency ω_k and solving the eigenvalue problem gives the Bloch vector $\mathbf{q}$ and the corresponding eigenmode. This also allows for an efficient computation of isofrequency contours and density of states at any desired frequency without the need to compute the complete band structure which is commonly done in other computational methods [33].

III. RESULTS

We first discuss the band structure of a square lattice of two-level atoms as shown in Fig. 1(a). For the SPP mode, we choose as an example the surface plasmon frequency lying in the infrared region $\hbar\omega_{sp} = 0.1$ eV. There have been many realizations of highly confined SPP mode with low propagation loss in conventional noble metals and in 2D materials such as graphene and hBN in the infrared spectrum [53,60–63]. We use the following parameters for the quantum dots (Here, we interchangeably use atoms and quantum dots.) with ground and excited state wave functions described by Eq. (8): Radius $a = 10$ nm, length $L = 3.35$ nm, such that the atomic transition energy $\hbar\Omega = (E_e - E_g)$ lies close to the surface plasmon energy $\hbar\omega_{sp}$ with a small detuning $\hbar\Delta\omega = \hbar(\Omega - \omega_{sp}) = -0.15$ meV. The detuning value can be adjusted by applying a small static field. The quantum dots are placed at a height $h = 200$ nm. The spectrum for a single SPP photon scattering by an isolated atom is shown in Fig. 1(c), which plots the scattering coefficient squared $|b_0|^2$ and excited state amplitude squared $|e_{k,0}|^2$ as a function of frequency ω. Here, $\mathbf{k}$ is the in-plane wave vector of the incident photon corresponding to a SPP 2D plane wave of the form $e^{i\mathbf{k}\cdot\mathbf{r}}$. As discussed previously, because of the azimuthal symmetry of the electron wave functions, only the $m = 0$ angular momentum component of the incident wave is scattered [Eqs. (10a) and (10b)]. Thus, the scattering coefficient is independent of the angle of incidence and only depends on the SPP wave-vector magnitude k. This enables us to plot the scattering coefficients as a function of frequency as there is a one-to-one correspondence between k and ω [Eq. (2)]. The scattering spectrum in Fig. 1(c) has a single-peaked Lorentzian line shape which is the expected behavior in the Markovian regime at relatively large distances h between the atom and the surface supporting the SPP mode. We also observe a small Lamb shift which is the difference between the bare atomic transition frequency and the resonant frequency in the spectrum.

Figure 2 shows the band structure for a square lattice of two-level atoms with a period $D = 200$ nm. Figure 2(a) plots the dispersion relation along the boundary of the irreducible Brillouin zone ΓXM. We see a bandgap between
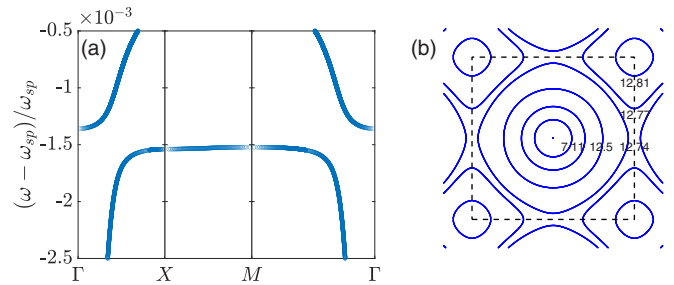
FIG. 2. (a) Band structure, and (b) Isofrequency contours of a square lattice of single atoms with period $D = 200$ nm. The numbers labeling the isofrequency contours represent the SPP wave-vector magnitude ck/ω_{sp}.

the first two bands. The bandgap is in agreement with the frequency range where an isolated atom shows significant scattering as shown in Fig. 1(c). In general, the width of the bandgap depends on the periodicity of the lattice and the scattering linewidth of an isolated atom. Figure 2(b) shows isofrequency contours in the first Brillouin zone for frequencies corresponding to the lower band. Close to the Γ point, we observe circular contours which is a consequence of the underlying isotropic SPP dispersion. The deviation of the contours from a circle close to the Brillouin zone boundary is reminiscent of similar isofrequency contours in 2D photonic crystals [33,64,65].

A. Slow light and EIT-like unit cell

Having discussed the case of a square lattice of two-level atoms, we now propose a scheme to slow light by obtaining an isolated band with a very small slope across the Brillouin zone. Towards this end, we first design an isolated unit cell such that it exhibits EIT-like spectrum with a "zero scattering frequency". This could be achieved using two similar vertically stacked quantum dots in a unit cell, henceforth referred to as an EIT-like cell, as discussed in our previous work [46]. By making the quantum dots aligned horizontally but displaced vertically as shown in Fig. 3(a), it is possible by destructive interference of their scattered fields, to completely cancel the net scattering at a desired frequency which results in an EIT-like behavior. The two atoms have identical wave functions as described by Eq. (8) and slightly different
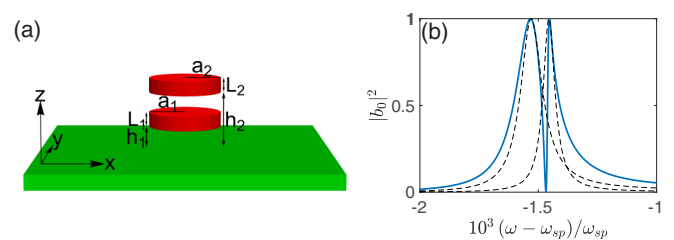
FIG. 3. (a) EIT-like unit cell of a square lattice with period D, comprised of two vertically stacked quantum dots/atoms coupled to SPP mode, (b) Scattering spectrum of an isolated unit cell with two atoms. The solid blue and the two dashed black curves plot the scattered field amplitude squared $|b_0|^2$ for the EIT-like cell and isolated atoms, respectively.
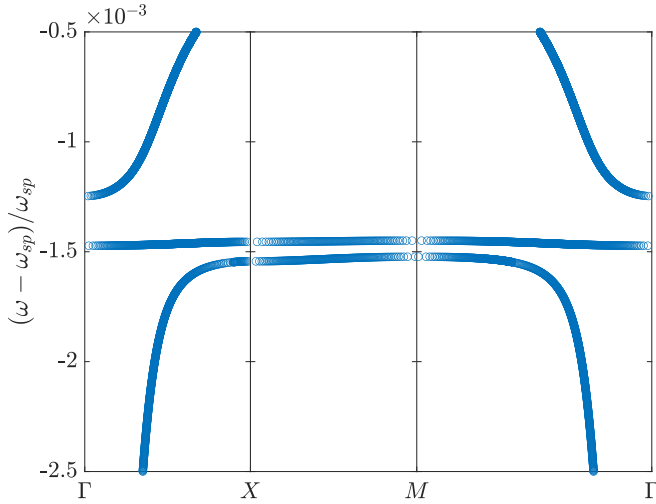
FIG. 4. Band structure of a square lattice of EIT-like cells with period $D = 200$ nm.

detuning values $\hbar\Delta\omega_1 = -0.15$ meV, $\hbar\Delta\omega_2 = -0.145$ meV. The atoms are placed at heights $h_1 = 200$ nm and $h_2 = 250$ nm. Note that the EIT-like cell with these parameters is identical to the single atom unit cell discussed above but with an extra second atom. The height and the detuning value for the second atom are chosen to get a slightly frequency-shifted scattering spectrum so as to make the EIT-like frequency (zero scattering frequency) lie inside the bandgap obtained for the lattice of single atoms [Fig. 2(a)]. Since the scattering is negligible at frequencies near the EIT-like point, one expects to observe propagating Bloch states in this narrow frequency range inside the bandgap. The following discussion clarifies this point.

Figure 3(b) shows the scattering spectrum for an isolated EIT-like cell. Similar to the previous case for plane wave scattering by a single atom, as a consequence of azimuthal symmetry, only the $m = 0$ angular momentum component is scattered. Thus, the scattering behavior is completely specified by the only nonzero scattering coefficient b_0. The solid blue curve in Fig. 3(b) plots $|b_0|^2$ as a function of frequency of the incident SPP photon. We observe an EIT-like spectrum with two resonant peaks and zero scattering at a frequency in between. The dotted black curves correspond to the scattering spectrum for the individual atoms which is similar to the Lorentzian spectrum observed in Fig. 1(c).

Having obtained the scattering coefficients for an isolated EIT-like cell, we can now obtain the band structure for a square lattice of EIT-like cells using the DtN technique. Figure 4 shows the band structure for a lattice period $D = 200$ nm. As before, we only show the dispersion relation along the boundary of the irreducible Brillouin zone. In the same frequency range as Fig. 2, we observe an extra band with a small slope throughout the Brillouin zone and separated from the other two bands by a finite gap. The other two bands are similar to those observed for the lattice of single atoms in Fig. 2(a). The position of the flat band is centered around the EIT-like frequency for the isolated EIT-like cell shown in Fig. 3(b). The slope of the flat band depends on the slope of the scattering spectrum near the EIT-like frequency [Fig. 3(b)]

and we achieve here, on average, a group velocity magnitude of 165 m/s which is smaller than the bare SPP mode group velocity by almost a factor of 400. A sharper transition in the scattering spectrum near the EIT-like frequency will result in a smaller slope for the flat band. This can be achieved by having a narrower linewidth scattering response for one of the atoms in the EIT-like cell.

Besides having a small slope for the flat band to exhibit a small group velocity, it is also equally important to have the flat band well isolated from the other bands through a large bandgap to prevent interband scattering/coupling. We define the following metric to quantify the performance of the flat band:

$$F = \frac{\min\{\Delta\omega_{\text{gap}}\}}{\Delta\omega_{FB}}, \tag{20}$$

where, $\Delta\omega_{FB}$ is the width of the flat band and $\min\{\Delta\omega_{\text{gap}}\}$ is the frequency separation between the flat band and the nearest band. Having a large F allows for an efficient adiabatic bandwidth compression of a photon pulse through dynamic time modulation of the slope of the flat band [41,66]. For the bands shown in Fig. 4, $F = 2.16$, which we would like to improve. As discussed earlier, one way to reduce the slope and thus enhance F is to make the scattering spectrum of one of the atoms in the EIT-like cell narrower by weakening the atom-SPP coupling strength $V_{\mathbf{k}}$. A trivial way to do this is to move the second atom further away from the surface supporting the SPP mode, i.e., increasing h_2. Unfortunately, this approach is limited because even though the atom-SPP coupling strength decreases exponentially with h_2, the coupling to the free-space modes does not change appreciably. At sufficiently large h_2, the coupling of the atom to the free-space modes becomes comparable to the coupling to the SPP mode leading to considerable loss due to emission into free space modes. Thus, F cannot be improved significantly using this approach.

B. Even slower light and Fano-like unit cell

To improve F, we focus on other degrees of freedom available to us for optimization, namely tailoring the electron wave functions of the quantum dots. The goal is to obtain a much narrower spectrum for the second atom. Here, we propose to achieve it via proper design of the ground ($\psi_g^{(2)}(\mathbf{r}, z)$) and excited ($\psi_e^{(2)}(\mathbf{r}, z)$) state wave functions of the second quantum dot as

$$\psi_g^{(2)}(\mathbf{r}, z) = \sqrt{\frac{2}{L_2}} \sin\frac{\pi(z - h_2)}{L_2}$$
$$\times \frac{1}{\sqrt{\pi}a_2 J_1(j_0)} J_0(j_0 r/a_2)\Theta(r, z), \tag{21a}$$

$$\psi_e^{(2)}(\mathbf{r}, z) = \sqrt{\frac{2}{L_2}} \sin\frac{2\pi(z - h_2)}{L_2}$$
$$\times \frac{1}{\sqrt{\pi}a_2 J_1(j_1)} J_0(j_1 r/a_2)\Theta(r, z). \tag{21b}$$

The transition dipole moment $\langle\psi_e^{(2)}| - e\mathbf{r}|\psi_g^{(2)}\rangle$ for these wave functions is zero making the free-space electric
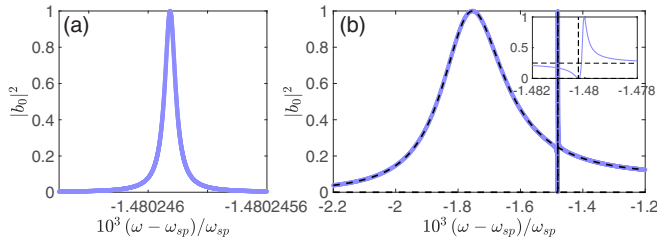
FIG. 5. Scattering spectrum of an isolated (a) second atom, (b) Fano-like cell with two atoms. The solid blue and the two dashed black curves plot the scattered field amplitude squared $|b_0|^2$ for the Fano-like cell and the isolated atoms, respectively. The inset in (b) shows a zoomed-in view of the scattering spectrum near the zero scattering frequency.
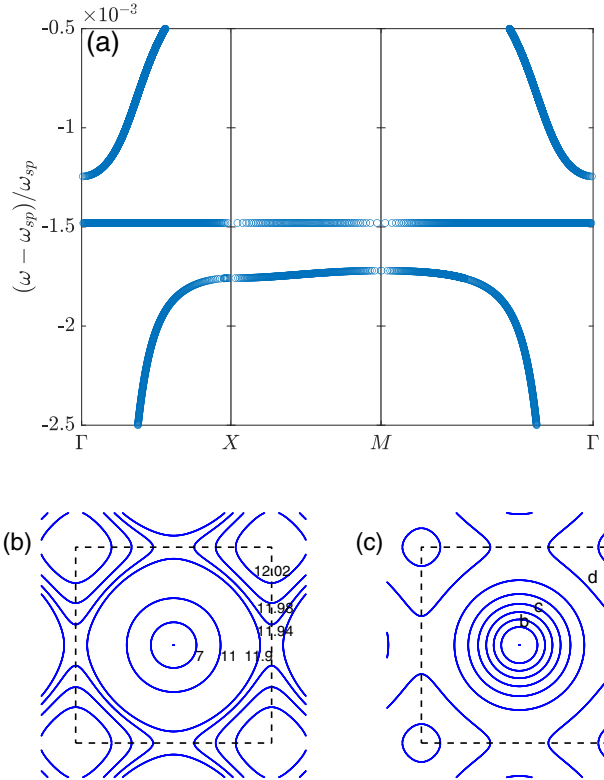

FIG. 6. (a) Band structure, and (b), (c) Isofrequency contours of a square lattice of Fano-like cells with period $D = 200$ nm. The numbers labeling the isofrequency contours in (b) represent the SPP wave-vector magnitude ck/ω_{sp}. The isofrequency contours in (c) are spaced at equal frequency intervals of $7 \times 10^{-8} \omega_{sp}$ except for the spacing between the contours labeled d and e being $3 \times 10^{-8} \omega_{sp}$. Contour labeled e has frequency $\omega - \omega_{sp} = -1.48 \times 10^{-3} \omega_{sp}$.

dipole transition forbidden. The excited state to the ground state transition rate due to electric quadrupole or magnetic dipole transitions in free space is very low. However, due to the stronger coupling with the SPP mode, one can make these higher order multipole transitions much faster. Thus, one can obtain a narrow linewidth for the single SPP scattering while keeping the photon loss to the free-space modes negligible. Figure 5(a) shows the scattering spectrum for such an isolated single quantum dot with wave functions given by Eq. (21). The quantum dot has radius $a_2 = 10.5$ nm, length $L_2 = 3.5$ nm, detuning $\hbar\Delta\omega_2 = -0.148$ meV, and is placed at height $h_2 = 50$ nm above the surface. The scattering coefficient squared $|b_0|^2$ has a Lorentzian line shape with a linewidth which is almost five orders of magnitude narrower as compared to the previous case [Fig. 3(b)], even at a much closer distance h_2.

Figure 5(b) plots the scattering coefficient for the new isolated cell with two atoms [Fig. 3(a)]. We refer this structure as a Fano-like cell because we are coupling here two resonances with extremely different linewidths, which yields the well-known asymmetric Fano resonance line shape as discussed below. The solid blue curve in Fig. 5(b) shows $|b_0|^2$ of the isolated Fano-like cell as a function of frequency of the incident SPP photon. The dashed black curves correspond to the scattering coefficients for the individual atoms. As compared to the previous EIT-like cell, the first atom still has the same wave functions [Eq. (8)], identical dimensions ($a_1 = 10$ nm, $L_1 = 3.35$ nm), but has zero detuning ($\hbar\Delta\omega_1 = 0$) and is placed closer to the surface ($h_1 = 60$ nm). These parameters were chosen to obtain a broader linewidth for the first atom which, as we will see later, results in a larger bandgap for the same lattice period. The spectrum corresponding to the first atom is much broader and substantially deviates from a symmetric Lorentzian, which is attributed to the frequency dependence of atom-field coupling strength $V_{\mathbf{k}}$, which changes appreciably over the linewidth resulting in non-Markovian behavior [54]. The second atom is identical to the one discussed in the previous paragraph. On this scale the scattering spectrum corresponding to the second atom appears to have almost zero width. This makes the transition near the zero scattering frequency much sharper as compared to the one shown in Fig. 3(b). The inset shows a zoomed-in view of the spectrum near the zero scattering frequency and clearly shows an asymmetric Fano resonance line shape. The zero in the

net scattering cross section results from Fano interference between a background scattering (broader resonance in the first atom) and a resonant scattering pathway (narrow resonance in the second atom) [67–69].

Figure 6 shows the band structure for a square lattice of such Fano-like cells with period $D = 200$ nm. The dispersion relation plotted in Fig. 6(a) is similar to the one shown in Fig. 4, but the flat band has a much smaller slope and is optimally positioned at the middle of the bandgap. Here, the average group velocity magnitude is around 4 m/s which is more than four orders of magnitude smaller than the bare SPP velocity. As a result, we obtain $F = 430$, more than two orders of magnitude larger than the previous case. The optimal positioning of the flat band is achieved by choosing an appropriate detuning value for the second atom ($\hbar\Delta\omega_2$), which ensures that the zero scattering frequency and thus consequently the flat band lies in the middle of the bandgap. Figures 6(b) and 6(c) plot a few isofrequency contours in the first Brillouin zone for frequencies corresponding to the first (lowest) and the flat bands, respectively.

C. Single photon scattering from finite size lattices

So far, we have based our discussion on band structures, which is valid for an infinite lattice and can only
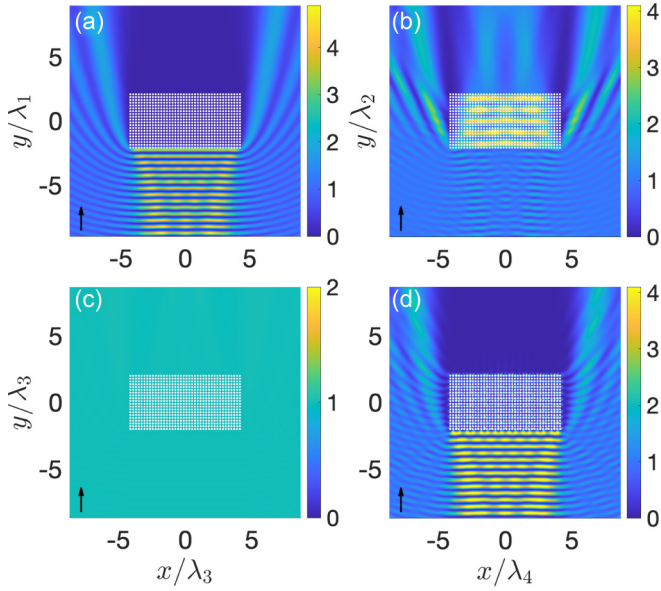
FIG. 7. Total field plots for scattering of a y-propagating SPP plane wave from a finite square lattice of Fano-like cells for frequency lying (a) within the band gap $k = 13.5\,k_{sp}$, (b), (c), (d) on the flat band as marked on Fig. 6(c), with Fabry-Perot resonance in (b), cloaking (transparency) from zero scattering in (c), and 100% reflection in (d). The field distribution is normalized such that the incident plane wave has unit amplitude.

approximately be realized in practice. Here, we briefly discuss the case of finite lattices realized with hundreds of unit cells. For the finite system, the DtN technique is no longer applicable, and the computational technique used for the following results was proposed in our recent work [46]. It involves first computing the scattering from an isolated atom/cell and then expressing the scattered field from the finite lattice in terms of the scattered field modes from each unit cell. The lattice consists of a 40×20 array of the Fano-like cells discussed previously in Figs. 5 and 6. Figure 7 shows the total field plots for an incident photon in the SPP 2D plane wave mode for different frequencies. The black arrow indicates the direction of incidence and the white dots mark the position of the atoms in the lattice. Figure 7(a) is plotted at a frequency $\omega - \omega_{sp} = -1.37 \times 10^{-3} \omega_{sp}$ which lies inside the bandgap of the infinite lattice (Fig. 6). As expected, the finite lattice is an ideal single photon mirror for frequencies within the bandgap. Figures 7(b), 7(c), and 7(d) are plotted at almost the same frequency $\omega - \omega_{sp} = -1.48 \times 10^{-3} \omega_{sp}$ lying on the flat band and marked as b, c and d, respectively, on the isofrequency plot in Fig. 6(c). Despite this negligible frequency difference and the same direction of incidence, the three field plots are very different. This large contrast arises from the almost zero slope of the dispersion relation in the flat band which leads to the excitation of Bloch waves with very different wave vectors inside the lattice even for a small frequency difference of the incident photon as seen from the isofrequency plot [Fig. 6(c)]. Ignoring the obvious diffraction effects at the edges, the incident wave with $k_x = 0$ couples efficiently with the lattice Bloch mode with $q_x = 0$ in Fig. 7(b) and exhibits a significant transmission due to Fabry-Perot-like resonance, whereas the

absence of such a Bloch mode with $q_x = 0$ leads to negligible coupling and almost complete reflection in Fig. 7(d). The high reflection in Fig. 7(d) is qualitatively different from that in Fig. 7(a) which is due to a lack of propagating Bloch states inside the bandgap. Here, it may be possible to get significant transmission at the same frequency by changing the angle of incidence. In Fig. 7(c), the lattice can be seen to be completely cloaked (transparent) as the frequency of the incident photon is equal to the zero scattering frequency [Fig. 5(b)]. Thus, in a small frequency range we observe Fabry-Perot resonance, transparency, and complete reflection.

One could also manipulate the slow surface plasmons to exhibit interesting phenomena such as superprism effect, supercollimation and negative refraction through appropriately designed isofrequency contours [65,70–76]. For instance, in Fig. 6(c), the contour labeled d and centered at M point has fairly sharp corners and flat edges. By coupling the incident wave to lattice Bloch modes near these corners, one can quickly switch from one side of the corner to the other. This results in a large change in group velocity and thus angle of refraction inside the lattice for a very small change in frequency or angle of incidence, and is termed as superprism effect [70,71]. Similarly, by coupling light into the flat edge of the contour, one could negate the effect of diffraction since the group velocity for all the points on the flat contour point in the same direction. Thus such a beam inside the lattice would spread out very slowly, which results in a supercollimation effect [72–74]. Finally, at frequency $\omega - \omega_{sp} = -1.48 \times 10^{-3} \omega_{sp}$, the contour near M labeled e in Fig. 6(c), assumes a circular shape, but the radius of the circle decreases as the frequency increases. This contour can be used to demonstrate negative refraction and flat lens [75,76].

IV. CONCLUSION

We have proposed a DtN map based technique to compute the properties of a 2D atomic lattice coupled to an electromagnetic bath with 2D continuum of photonic states. The proposed model is general and can efficiently capture the non-Markovian dynamics as well as narrow bandwidth features associated with the electromagnetic environment. Subsequently, we designed an atomic lattice with an isolated flat band which could be employed to slow light and further enhance light-matter interaction. This is a realization of group velocity reduction by several orders of magnitudes in a 2D system, using only two-level atoms. We also optimized the performance of the proposed lattice of quantum dots through proper design of the electron wave functions. Finally, we pointed out the possibility of manipulating single photons using a finite lattice of atoms, to exhibit interesting effects associated with perfect mirror, superprism, supercollimation, and negative refraction.

[1] P. Goy, J. M. Raimond, M. Gross, and S. Haroche, Observation of Cavity-Enhanced Single-Atom Spontaneous Emission, Phys. Rev. Lett. **50**, 1903 (1983).

[2] D. J. Heinzen, J. J. Childs, J. E. Thomas, and M. S. Feld, Enhanced and Inhibited Visible Spontaneous Emission by Atoms in a Confocal Resonator, Phys. Rev. Lett. **58**, 1320 (1987).

[3] R. G. Hulet, E. S. Hilfer, and D. Kleppner, Inhibited Spontaneous Emission by a Rydberg Atom, Phys. Rev. Lett. **55**, 2137 (1985).

[4] N. Rivera, I. Kaminer, B. Zhen, J. D. Joannopoulos, and M. Soljačić, Shrinking light to allow forbidden transitions on the atomic scale, Science **353**, 263 (2016).

[5] P. K. Jain, D. Ghosh, R. Baer, E. Rabani, and A. P. Alivisatos, Near-field manipulation of spectroscopic selection rules on the nanoscale, Proc. Natl. Acad. Sci. USA **109**, 8016 (2012).

[6] T. Neuman, R. Esteban, D. Casanova, F. J. García-Vidal, and J. Aizpurua, Coupling of molecular emitters and plasmonic cavities beyond the point-dipole approximation, Nano Lett. **18**, 2358 (2018).

[7] R. Filter, S. Mühlig, T. Eichelkraut, C. Rockstuhl, and F. Lederer, Controlling the dynamics of quantum mechanical systems sustaining dipole-forbidden transitions via optical nanoantennas, Phys. Rev. B **86**, 035404 (2012).

[8] K. M. Birnbaum, A. Boca, R. Miller, A. D. Boozer, T. E. Northup, and H. J. Kimble, Photon blockade in an optical cavity with one trapped atom, Nature (London) **436**, 87 (2005).

[9] A. V. Gorshkov, J. Otterbach, M. Fleischhauer, T. Pohl, and M. D. Lukin, Photon-Photon Interactions via Rydberg Blockade, Phys. Rev. Lett. **107**, 133602 (2011).

[10] R. H. Dicke, Coherence in spontaneous radiation processes, Phys. Rev. **93**, 99 (1954).

[11] R. G. DeVoe and R. G. Brewer, Observation of Superradiant and Subradiant Spontaneous Emission of Two Trapped Ions, Phys. Rev. Lett. **76**, 2049 (1996).

[12] T. Shi, Y. H. Wu, A. González-Tudela, and J. I. Cirac, Bound States in Boson Impurity Models, Phys. Rev. X **6**, 021027 (2016).

[13] J. T. Shen and S. Fan, Strongly correlated multiparticle transport in one dimension through a quantum impurity, Phys. Rev. A **76**, 062709 (2007).

[14] L. Guo, A. F. Kockum, F. Marquardt, and G. Johansson, Oscillating bound states for a giant atom, Phys. Rev. Research **2**, 043014 (2020).

[15] S. E. Harris, J. E. Field, and A. Imamoğlu, Nonlinear Optical Processes using Electromagnetically Induced Transparency, Phys. Rev. Lett. **64**, 1107 (1990).

[16] K. J. Boller, A. Imamoğlu, and S. E. Harris, Observation of Electromagnetically Induced Transparency, Phys. Rev. Lett. **66**, 2593 (1991).

[17] M. Fleischhauer, A. Imamoglu, and J. P. Marangos, Electromagnetically induced transparency: Optics in coherent media, Rev. Mod. Phys. **77**, 633 (2005).

[18] G. Facchinetti, S. D. Jenkins, and J. Ruostekoski, Storing Light with Subradiant Correlations in Arrays of Atoms, Phys. Rev. Lett. **117**, 243601 (2016).

[19] A. Asenjo-Garcia, M. Moreno-Cardoner, A. Albrecht, H. J. Kimble, and D. E. Chang, Exponential Improvement in Photon Storage Fidelities using Subradiance and "Selective Radiance" in Atomic Arrays, Phys. Rev. X **7**, 031024 (2017).

[20] S. D. Jenkins, J. Ruostekoski, N. Papasimakis, S. Savo, and N. I. Zheludev, Many-Body Subradiant Excitations in Metamaterial Arrays: Experiment and Theory, Phys. Rev. Lett. **119**, 053901 (2017).

[21] R. J. Bettles, S. A. Gardiner, and C. S. Adams, Enhanced Optical Cross Section Via Collective Coupling of Atomic Dipoles in a 2D Array, Phys. Rev. Lett. **116**, 103602 (2016).

[22] E. Shahmoon, D. S. Wild, M. D. Lukin, and S. F. Yelin, Cooperative Resonances in Light Scattering from Two-Dimensional Atomic Arrays, Phys. Rev. Lett. **118**, 113601 (2017).

[23] J. Perczel, J. Borregaard, D. E. Chang, H. Pichler, S. F. Yelin, P. Zoller, and M. D. Lukin, Topological Quantum Optics in Two-Dimensional Atomic Arrays, Phys. Rev. Lett. **119**, 023603 (2017).

[24] R. J. Bettles, J. Minář, C. S. Adams, I. Lesanovsky, and B. Olmos, Topological properties of a dense atomic lattice gas, Phys. Rev. A **96**, 041603(R) (2017).

[25] D. Jaksch, C. Bruder, J. I. Cirac, C. W. Gardiner, and P. Zoller, Cold Bosonic Atoms in Optical Lattices, Phys. Rev. Lett. **81**, 3108 (1998).

[26] I. Bloch, Ultracold quantum gases in optical lattices, Nat. Phys. **1**, 23 (2005).

[27] C. Santori, P. E. Barclay, K. M. C. Fu, R. G. Beausoleil, S. Spillane, and M. Fisch, Nanophotonics for quantum optics using nitrogen-vacancy centers in diamond, Nanotechnology **21**, 274008 (2010).

[28] J. Majer, J. M. Chow, J. M. Gambetta, J. Koch, B. R. Johnson, J. A. Schreier, L. Frunzio, D. I. Schuster, A. A. Houck, A. Wallraff, and A. Blais, Coupling superconducting qubits via a cavity bus, Nature (London) **449**, 443 (2007).

[29] J. M. Gerard and B. Gayral, InAs quantum dots: Artificial atoms for solid-state cavity-quantum electrodynamics, Physica E: Low-Dimens. Syst. Nanostruct. **9**, 131 (2001).

[30] J. Perczel, J. Borregaard, D. E. Chang, H. Pichler, S. F. Yelin, P. Zoller, and M. D. Lukin, Photonic band structure of two-dimensional atomic lattices, Phys. Rev. A **96**, 063801 (2017).

[31] J. Yuan and Y. Y. Lu, Photonic bandgap calculations with Dirichlet-to-Neumann maps, J. Opt. Soc. Am. A **23**, 3217 (2006).

[32] J. Yuan and Y. Y. Lu, Computing photonic band structures by Dirichlet-to-Neumann maps: The triangular lattice, Opt. Commun. **273**, 114 (2007).

[33] V. Liu and S. Fan, Efficient computation of equifrequency surfaces and density of states in photonic crystals using Dirichlet-to-Neumann maps, J. Opt. Soc. Am. B **28**, 1837 (2011).

[34] L. Zhao, K. L. Kelly, and G. C. Schatz, The extinction spectra of silver nanoparticle arrays: Influence of array structure on plasmon resonance wavelength and width, J. Phys. Chem. B **107**, 7343 (2003).

[35] S. Zou and G. C. Schatz, Narrow plasmonic/photonic extinction and scattering line shapes for one and two dimensional silver nanoparticle arrays, J. Chem. Phys. **121**, 12606 (2004).

[36] C. L. Holloway, D. C. Love, E. F. Kuester, J. A. Gordon, and D. A. Hill, Use of generalized sheet transition conditions to model guided waves on metasurfaces/metafilms, IEEE Trans. Antennas Propag. **60**, 5173 (2012).

[37] A. Kasapi, M. Jain, G. Y. Yin, and S. E. Harris, Electromagnetically Induced Transparency: Propagation Dynamics, Phys. Rev. Lett. **74**, 2447 (1995).

[38] L. V. Hau, S. E. Harris, Z. Dutton, and C. H. Behroozi, Light speed reduction to 17 metres per second in an ultracold atomic gas, Nature (London) **397**, 594 (1999).

[39] A. V. Turukhin, V. S. Sudarshanam, M. S. Shahriar, J. A. Musser, B. S. Ham, and P. R. Hemmer, Observation of Ultra-slow and Stored Light Pulses in a Solid, Phys. Rev. Lett. **88**, 023602 (2001).

[40] M. Fleischhauer and M. D. Lukin, Dark-State Polaritons in Electromagnetically Induced Transparency, Phys. Rev. Lett. **84**, 5094 (2000).

[41] M. F. Yanik, W. Suh, Z. Wang, and S. Fan, Stopping Light in a Waveguide with an All-Optical Analog of Electromagnetically induced Transparency, Phys. Rev. Lett. **93**, 233903 (2004).

[42] J. T. Shen and S. Fan, Coherent photon transport from spontaneous emission in one-dimensional waveguides, Opt. Lett. **30**, 2001 (2005).

[43] L. Zhou, Z. R. Gong, Yu-xi Liu, C. P. Sun, and F. Nori, Controllable Scattering of a Single Photon Inside a One-Dimensional Resonator Waveguide, Phys. Rev. Lett. **101**, 100501 (2008).

[44] J. T. Shen and S. Fan, Input-output formalism for few-photon transport in one-dimensional nanophotonic waveguides coupled to a qubit, Phys. Rev. A **82**, 063821 (2010).

[45] J. T. Shen and S. Fan, Quantum scattering theory of a single-photon Fock state in three-dimensional spaces, Opt. Lett. **41**, 4166 (2016).

[46] Rituraj, M. Orenstein, and S. Fan, Scattering of a single plasmon polariton by multiple atoms for in-plane control of light, Nanophotonics **10**, 579 (2021).

[47] B. A. Ferreira, B. Amorim, A. J. Chaves, and N. M. R. Peres, Quantization of graphene plasmons, Phys. Rev. A **101**, 033817 (2020).

[48] M. S. Tame, K. R. McEnery, Ş. K. Özdemir, J. Lee, S. A. Maier, and M. S. Kim, Quantum plasmonics, Nat. Phys. **9**, 329 (2013).

[49] A. Archambault, F. Marquier, J. J. Greffet, and C. Arnold, Quantum theory of spontaneous and stimulated emission of surface plasmons, Phys. Rev. B **82**, 035411 (2010).

[50] K. J. Blow, R. Loudon, S. J. D. Phoenix, and T. J. Shepherd, Continuum fields in quantum optics, Phys. Rev. A **42**, 4102 (1990).

[51] E. N. Economou, Surface plasmons in thin films, Phys. Rev. **182**, 539 (1969).

[52] M. Jablan, H. Buljan, and M. Soljačić, Plasmonics in graphene at infrared frequencies, Phys. Rev. B **80**, 245435 (2009).

[53] M. Jablan, M. Soljačić, and H. Buljan, Plasmons in graphene: Fundamental properties and potential applications, Proc. IEEE **101**, 1689 (2013).

[54] Rituraj, M. Orenstein, and S. Fan, Two-level quantum system as a macroscopic scatterer for ultraconfined two-dimensional photonic modes, Phys. Rev. A **102**, 013717 (2020).

[55] M. O. Scully and M S. Zubairy, *Quantum Optics* (Cambridge University Press, Cambridge, 1999).

[56] D. F. Walls and G. J. Milburn, *Quantum Optics* (Springer Science & Business Media, New York, 2007).

[57] E. A. Power and T. Thirunamachandran, On the nature of the Hamiltonian for the interaction of radiation with atoms and molecules: (e/mc)p.A,-μ.E, and all that, Am. J. Phys. **46**, 370 (1978).

[58] V. I. Yudson and P. Reineker, Multiphoton scattering in a one-dimensional waveguide with resonant atoms, Phys. Rev. A **78**, 052713 (2008).

[59] A. S. Baltenkov and A. Z. Msezane, Electronic quantum confinement in cylindrical potential well, Eur. Phys. J. D **70**, 81 (2016).

[60] A. Woessner, M. B. Lundeberg, Y. Gao, A. Principi, P. Alonso-González, M. Carrega, K. Watanabe, T. Taniguchi, G. Vignale, M. Polini, and J. Hone, Highly confined low-loss plasmons in graphene–boron nitride heterostructures, Nat. Mater. **14**, 421 (2015).

[61] Z. Fei, G. O. Andreev, W. Bao, L. M. Zhang, A. S. McLeod, C. Wang, M. K. Stewart, Z. Zhao, G. Dominguez, M. Thiemens, and M. M. Fogler, Infrared nanoscopy of Dirac plasmons at the graphene–SiO$_2$ interface, Nano Lett. **11**, 4701 (2011).

[62] I.-H. Lee, M. He, X. Zhang, Y. Luo, S. Liu, J. H. Edgar, K. Wang, P. Avouris, T. Low, J. D. Caldwell, and S.-H. Oh, Image polaritons in boron nitride for extreme polariton confinement with low losses, Nat. Commun. **11**, 3649 (2020).

[63] L. Wang, R. Chen, M. Xue, S. Liu, J. H. Edgar, and J. Chen, Manipulating phonon polaritons in low loss ^{11}B enriched hexagonal boron nitride with polarization control, Nanoscale **12**, 8188 (2020).

[64] D. N. Chigrin, S. Enoch, C. M. S. Torres, and G. Tayeb, Self-guiding in two-dimensional photonic crystals, Opt. Express **11**, 1203 (2003).

[65] J. D. Joannopoulos, S. G. Johnson, J. N. Winn, and R. D. Meade, Photonic crystals: Molding the flow of light, 2008.

[66] M. F. Yanik and S. Fan, Stopping Light all Optically, Phys. Rev. Lett. **92**, 083901 (2004).

[67] U. Fano, Effects of configuration interaction on intensities and phase shifts, Phys. Rev. **124**, 1866 (1961).

[68] M. F. Limonov, M. V. Rybin, A. N. Poddubny, and Y. S. Kivshar, Fano resonances in photonics, Nat. Photon. **11**, 543 (2017).

[69] S. Fan, W. Suh, and J. D. Joannopoulos, Temporal coupled-mode theory for the Fano resonance in optical resonators, J. Opt. Soc. Am. A **20**, 569 (2003).

[70] H. Kosaka, T. Kawashima, A. Tomita, M. Notomi, T. Tamamura, T. Sato, and S. Kawakami, Superprism phenomena in photonic crystals, Phys. Rev. B **58**, R10096(R) (1998).

[71] L. Wu, M. Mazilu, T. Karle, and T. F. Krauss, Superprism phenomena in planar photonic crystals, IEEE J. Quantum Electron. **38**, 915 (2002).

[72] H. Kosaka, T. Kawashima, A. Tomita, M. Notomi, T. Tamamura, T. Sato, and S. Kawakami, Self-collimating phenomena in photonic crystals, Appl. Phys. Lett. **74**, 1212 (1999).

[73] L. Wu, M. Mazilu, and T. F. Krauss, Beam steering in planar-photonic crystals: From superprism to supercollimator, J. Lightwave Technol. **21**, 561 (2003).

[74] X. Yu and S. Fan, Bends and splitters for self-collimated beams in photonic crystals, Appl. Phys. Lett. **83**, 3251 (2003).

[75] M. Notomi, Theory of light propagation in strongly modulated photonic crystals: Refractionlike behavior in the vicinity of the photonic band gap, Phys. Rev. B **62**, 10696 (2000).

[76] C. Luo, S. G. Johnson, J. D. Joannopoulos, and J. B. Pendry, All-angle negative refraction without negative effective index, Phys. Rev. B **65**, 201104(R) (2002).